

Resonant Scanning Design and Control for Fast Spatial Sampling

Zhanghao Sun^{1,*}, Ronald Quan¹, and Olav Solgaard¹

¹Stanford University, Electrical Engineering, Stanford, CA, 94305, US

*zhsun@stanford.edu

ABSTRACT

Two-dimensional, resonant scanners have been utilized in a large variety of imaging modules due to their compact form, low power consumption, large angular range, and high speed. However, resonant scanners have problems with non-optimal and inflexible scanning patterns and inherent phase uncertainty, which limit practical applications. Here we propose methods for optimized design and control of the scanning trajectory of two-dimensional resonant scanners under various physical constraints, including high frame-rate and limited actuation amplitude. First, we propose an analytical design rule for uniform spatial sampling. We demonstrate theoretically and experimentally that by expanding the design space, the proposed designs outperform previous designs in terms of scanning range and fill factor. Second, we show that we can create flexible scanning patterns that allow focusing on user-defined Regions-of-Interest (RoI) by modulation of the scanning parameters. The scanning parameters are found by an optimization algorithm. In simulations, we demonstrate the benefits of these designs with standard metrics and higher-level computer vision tasks (LiDAR odometry and 3D object detection). Finally, we experimentally implement and verify both unmodulated and modulated scanning modes using a two-dimensional, resonant MEMS scanner. Central to the implementations is high bandwidth monitoring of the phase of the angular scans in both dimensions. This task is carried out with a position-sensitive photodetector combined with high-bandwidth electronics, enabling fast spatial sampling at $\sim 100\text{Hz}$ frame-rate.

Introduction

Recent years have seen the rapid development of LiDAR systems in robotics¹, autonomous vehicles²⁻⁴ and AR/VR applications⁵. Designing such systems require innovation in both hardware and software because real-time response requires fast information collection and processing. Optical scanners are commonly used in LiDAR to deflect laser beam(s) onto different sampling positions in space and acquire 3D data. Compared to conventional LiDAR scanners that operate in a raster scanning mode, redresonant scanners have a well-known advantage^{4,6-8}: the motion amplitude of a resonant scanner is $\sim Q$ times larger than that of a raster scanner, where Q is the quality factor of the resonant system^{4,6}. Resonant scanning also improve acquisition speed⁹⁻¹¹. Raster scanners acquire data in a prescribed sequential pattern that is limited by the speed of its slow axis. This results in slow spatial sampling that is unacceptable for many real-world applications, e.g. collision avoidance. In contrast, resonant scanners have high speed in both scanning axes, which is promising for high-speed information collection. To realize this advantage, resonant scanning patterns must be optimized such that information is acquired most efficiently within a short frame time, and their flexibility should be increased to allow situation-dependent, or "random" scanning patterns¹²⁻¹⁴.

Multiple scanning pattern designs have been proposed^{9,10,15-18}. Hwang et al. proposed a frequency selection rule for high frame-rate $\sim 10 - 100\text{Hz}$ operation^{15,16}. Tuma et al. applied optimization-based scanning trajectory design in scanning probe microscopy¹⁷, which operates at a lower frame-rate $\sim 1\text{Hz}$. Sub-frame sampling and updating were also proposed to boost the imaging updating rate^{6,9,10,19}. These designs tend to focus on actuation frequency selection while ignoring the phase. More recent work discussed both frequency and phase in scanning pattern design¹⁸, but they are limited to patterns that repeat in each frame. Moreover, none of these designs considered physical constraints such as actuation signal amplitude, which are important in real-world systems. The flexibility in scanning is also critical. As shown in reports on random-access scanning^{13,19,20}, scanning patterns that "focus" on specified Regions-of-Interest (RoI) meet data post-processing requirements better than uniform spatial sampling. Resonant scanners cannot abruptly change direction so truly random-access scanning is not possible, and traditionally resonant scanning has been optimized for uniform Field-of-View (FoV) coverage. Therefore, there is a need for approaches that allows RoI focused sampling using resonant scanners.

In this work, we demonstrate optimized designs for resonant scanning patterns with frame-rate $\sim 100\text{Hz}$ and limited actuation amplitudes. We first analyze uniform spatial sampling and introduce two metrics: fill-factor and scanning range. We show a trade-off between these two metrics in previous designs to motivate a better solution. An analytical design rule based on unmodulated scanning patterns (both axes have single-tone scanner motion) is proposed that takes various practical

35 considerations into account, such as high frame-rate, bounded actuation amplitude, scanner phase, and pattern repeating
 36 period. The proposed design out-performs previous designs that fail to consider these factors. Furthermore, we consider RoI-
 37 focused spatial sampling with resonant scanners. For this purpose, we demonstrate the utility of modulated resonant scanning
 38 patterns, which contain multiple frequency components around resonance. We develop a task-driven optimization framework
 39 to integrate scanning pattern design with post-processing on sampled 3D data.

40 To demonstrate the applications of designed resonant scanning patterns, we evaluate them in simulated 3D computer
 41 vision tasks including LiDAR odometry and object detection^{3,21-23} (section “Simulations”). To experimentally implement the
 42 designed patterns, we built a hardware prototype based on a MEMS scanner (section “Experiments”). We developed a control
 43 system that stabilizes the scanner phase during operation, which is critical for resonant mechanical systems^{8,24-28}. Compared
 44 to previously designed high-accuracy, narrow bandwidth phase control systems, the proposed method is wide-band and thus
 45 can operate in both unmodulated and modulated scanning modes.

46 Scanning Pattern Design

Laser beams reflected from scanners that are resonant in two orthogonal dimensions create "Lissajous patterns" that are
 described mathematically as follows:

$$\begin{cases} x(t) = A_x(t)\cos(2\pi f_x t + \phi_x(t)) \\ y(t) = A_y(t)\cos(2\pi f_y t + \phi_y(t)) \end{cases} \quad (1)$$

47 where f_x, f_y are the scanning frequencies, which are assumed to be close to resonant frequencies (f_x^r, f_y^r). The quantities
 48 $A_x(t), A_y(t)$ and $\phi_x(t), \phi_y(t)$ are the amplitudes and phases for the two scanning axes. When amplitudes and phases are
 49 static, both $x(t)$ and $y(t)$ are single-tone, and we denote the corresponding scanning patterns as unmodulated patterns. When
 50 small modulations (or, equivalently, multiple frequency components within resonance bandwidth) are added, we denote the
 51 corresponding scanning patterns as modulated patterns. To make the problem of optimizing the scanning patterns tractable,
 52 we make the following assumptions: (1) The amplitude of the actuation signal is bounded to reflect limitations on practical
 53 hardware. (2) We define a “frame time” T_{frame} (Note that this “frame time” is different from that used in previous literature^{9,10},
 54 we provide a comparison between these two concepts in Supplementary Information). Data collected within T_{frame} is used
 55 for evaluation or post-processing. We show that the bounded actuation amplitude and short frame time introduce a trade-off
 56 between two important metrics for spatial coverage: scanning range and fill factor, and motivates a better design rule. For
 57 simplicity, we choose $T_{frame} = m$, m being an integer between 6 to 9 (corresponding to 6 – 9ms T_{frame} with a 1kHz resonant
 58 scanner). (3) Without loss of generality, we assume resonant frequencies for the two scanning axes to be $f_x^r = r, f_y^r = 1$. In
 59 all the simulations, time is scaled by the scanning cycle in the y-axis and is dimensionless. To model typical MEMS scanners,
 60 we set a quality factor $Q = 20$. We also limit $r \in [1, 3]$. When r gets higher, the resonant scanning system gradually transitions
 61 to a raster-scanning system, with one axis scanning much slower than the other.

62 Unmodulated pattern design

We first analyze the spatial coverage of resonant scanning with bounded actuation amplitude. The goal is to achieve uniform
 spatial sampling in a normalized $[-1, 1] \times [-1, 1]$ Field-of-View (FoV). We use fill-factor and scanning range to characterize
 the spatial coverage of scanning patterns, following common usage in the literature^{15,18}. The fill factor characterizes the
 spatial coverage within a normalized scanning range. The range is determined by the scanning frequencies f_x, f_y and the
 transfer function of the resonant scanner $H_x(f_x), H_y(f_y)$. We quantify the two metrics in Equation 2:

$$\begin{cases} \text{fill-factor} \triangleq 2 - R_{max}, \quad \text{higher is better} \\ \text{scanning range} \triangleq H_x(f_x) \times H_y(f_y), \quad \text{higher is better} \\ H_x(f_x) = 1 / (\sqrt{((f_x/f_x^r)^2 - 1)^2 + (f_x/(f_x^r Q_x))^2}) Q_x \\ H_y(f_y) = 1 / (\sqrt{((f_y/f_y^r)^2 - 1)^2 + (f_y/(f_y^r Q_y))^2}) Q_y \end{cases} \quad (2)$$

63 We normalize the transfer function amplitudes to 1. Note that we only consider the amplitudes of the transfer functions
 64 because in the proposed control scheme, we directly monitor phase of the scanner motion, instead of the phase of the ac-
 65 tuation signals. Without loss of generality, we assume an ideal harmonic oscillator model for the resonant-scanner because
 66 the following analysis is only based on the band-pass characteristic, which are common to all resonant scanners. We also
 67 ignore cross-talk between x and y-axis motions in this simplified model. More discussions on cross-talk are presented in the
 68 discussion section. Similar to previous literature^{17,18}, fill-factor is defined through the radius of the largest inscribed circle
 69 R_{max} in the sampling pattern, as shown in Figure 1(a). To decouple the two metrics, the scanning pattern is normalized to
 70 $[-1, 1] \times [-1, 1]$ when calculating R_{max} (See Supplementary Information for details).

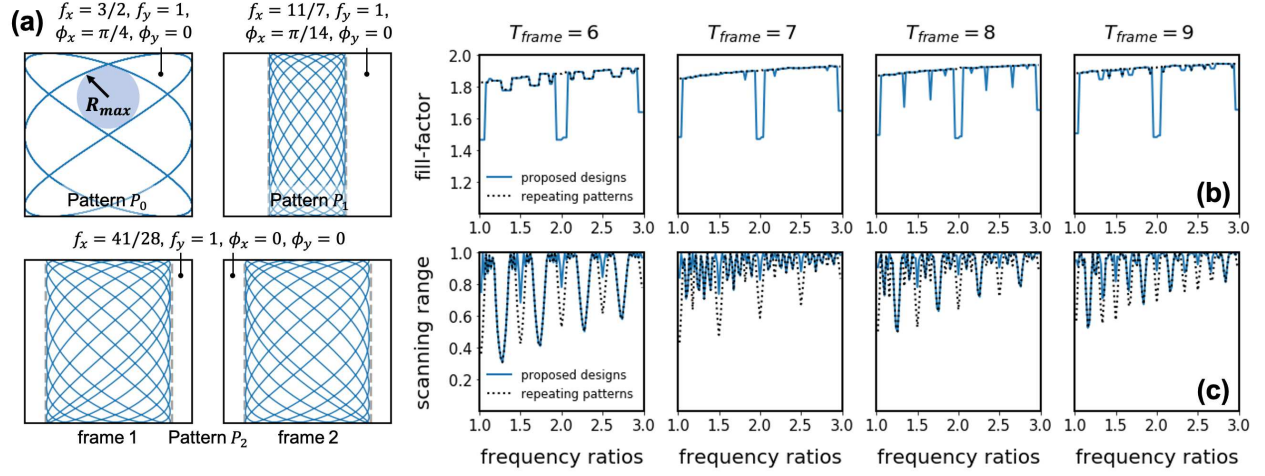


Figure 1. (a) Several scanning patterns for a resonant scanner with $f_x^r = 1.5$, $f_y^r = 1.0$ and $T_{frame} = 7$. Pattern P_0 is the on-resonance actuated pattern, Although it has large scanning range 1.0, fill-factor is low (0.63), as indicated by the radius of its largest inscribed circle. Pattern P_1 uses $f_x = 11/7$, $f_y = 1$, $\phi_x = \pi/14$, $\phi_y = 0$ as parameters. The fill-factor is improved to 0.89 but scanning range is reduced to 0.45. Pattern P_2 uses $f_x = 41/28$, $f_y = 1$, $\phi_x = 0$, $\phi_y = 0$, derived from design rule 1. It has fill-factor = 0.88 and scanning range = 0.74. (b),(c) Fill-factor/Scanning range with proposed design rule 1 (blue, solid) and repeating-pattern design rule¹⁸ (black, dashed), with different resonant frequency ratio and T_{frame} settings.

71 With bounded actuation amplitude, there is a fundamental trade-off between fill-factor and scanning range. As an example,
 72 we show several scanning patterns with $f_x^r = 1.5$, $f_y^r = 1$, $T_{frame} = 7$ in Figure 1(a). If we actuate on-resonance, the scanning
 73 range is at maximum (= 1.0), as shown in pattern P_0 . P_0 repeats in $t = 2$ with $\phi_x = \pi/4$, $\phi_y = 0$ and it samples on exactly
 74 the same trajectory multiple times within T_{frame} . This results in a low fill-factor = 1.63. On the other hand, if actuated off-
 75 resonance, with $f_x = 11/7$, $f_y = 1$, $\phi_x = \pi/14$, $\phi_y = 0$, the sampling pattern has high fill-factor = 1.89 (pattern P_1). However,
 76 off resonance actuation leads to large reduction in scanning range (= 0.45). In the lower part of Figure 1(a), we show another
 77 design (pattern P_2) with $f_x = 41/28$, $f_y = 1$, $\phi_x = \phi_y = 0$. P_2 has repeating period $14 = 2T_{frame}$. In each frame, P_2 has fill-factor
 78 1.88 and scanning range 0.74. The fill-factor is almost the same as that in P_1 and the scanning range (= 0.74) is $1.6\times$ larger.
 79 Therefore, with respect to spatial coverage within T_{frame} , we regard P_2 to be a better scanning pattern when compared to P_1 .

80 Previous resonant scanning pattern designs generally consider patterns that repeat in each $T_{frame} = m$, with $f_x = k/m$,
 81 $f_y = l/m$, $k, l \in \mathbb{Z}^{15,18}$ and we denote these “repeating patterns”. (Note that the “repeating”/“non-repeating” pattern definition
 82 here is different from the definition used in some previous literature^{9,10}, we provide a comparison between these two concepts
 83 in Supplementary Information) However, for a specific f_x^r, f_y^r, T_{frame} combination, there might not be a repeating pattern with
 84 (f_x, f_y) close enough to resonance. As in the example in Figure 1(a), it can be verified that P_1 is the repeating pattern with
 85 (f_x, f_y) closest to resonance, but P_1 still suffers from small scanning range. In this paper, we expand the design space by
 86 considering not only repeating patterns, but also patterns with repeating periods longer than T_{frame} , such as P_2 in the above
 87 example. We propose an analytical design rule in design rule 1 to maximize the scanning range while still achieve comparable
 88 fill-factors to that of repeating patterns (derivations are provided in Supplementary Information). In the design rule, we search
 89 over (f_x, f_y) pairs around the resonance frequencies (in a close-to-far order) until we find a pair that falls in one of three “good
 90 spatial coverage” cases: Case1, where the scanning pattern repeats in $2T_{frame}$ time and a criterion in line 4 of design rule 1 is
 91 met. Case2, where the scanning pattern repeats every T_{frame} with $\phi_x = \phi_y = 0$ and Case3, where the scanning pattern repeats in
 92 T_{frame} time with $\phi_x \neq \phi_y$. After the frequencies (f_x, f_y) are chosen, we determine the phases (ϕ_x, ϕ_y) . The three “good spatial
 93 coverage” cases and the criterion in line 4 of design rule 1 guarantee that the scanning trajectory does not repeat within T_{frame} .
 94 Mathematical proofs for the three “good spatial coverage” cases are provided in Supplementary Information. A very recent
 95 paper presented a design rule $|f_x \phi_y - f_y \phi_x| m = \pi/2$ to achieve a high fill-factor for repeating patterns¹⁸, which is similar to the
 96 phase selection rule in Case3. However, design rule 1 is more complete and performs better under the physical constraints.

97 Figures 1(b),(c) quantitatively show the dependence of fill-factor and scanning range on different settings $r \in [1, 3]$ and
 98 $T_{frame} \in [6, 9]$. The figures compare the metrics of our proposed designs (blue, solid) and traditional repeating pattern designs¹⁸
 99 (black, dashed), with a fixed actuation amplitude of 1 in all cases. The comparisons show that: (1) In most cases, the proposed
 100 designs have the same fill-factor as the repeating patterns, but larger scanning range. (2) When T_{frame} is shorter, and when m
 101 has more prime factors, the trade-off is generally less favorable. This is because with $f_x = k/4m$, the greatest common divider

Algorithm 1 Design rule 1: unmodulated scanning patterns

Input $f_x^r = r, f_y^r = 1, T_{frame} = m$ **Fixed** $f_y = 1, \phi_y = 0$ **Output** f_x, ϕ_x

```
1:  $k^* = \underset{k}{\operatorname{argmin}} |\frac{k}{4m} - r|$ , initial searching space for k is all positive integer numbers.
2: while TRUE do ▷ Loop until find solution
3:   if  $\operatorname{GCD}(k^*, 4m) == 1$  then ▷ GCD: the greatest common divider
4:     if  $\operatorname{mod}(k^*n, 4m) \neq \pm 1, n \in \{[m/2], [m/2] + 1, \dots, 3[m/2]\}$  then
5:       return  $f_x = k^*/4m, \phi_x = 0$  ▷ Case1
6:     else ▷ Choose a sub-optimal k, continue loop
7:       remove current  $k^*$  from searching space
8:        $k^* = \underset{k}{\operatorname{argmin}} |\frac{k}{4m} - r|$ 
9:     if  $\operatorname{GCD}(k^*, 4m) == 2$  then
10:      return  $f_x = k^*/4m, \phi_x = 0$ , ▷ Case2
11:    if  $\operatorname{GCD}(k^*, 4m) == 4$  then
12:      return  $f_x = k^*/4m, \phi_x = \pi/(2m)$ , ▷ Case3
13:    else ▷ Choose a sub-optimal k, continue loop
14:      remove current  $k^*$  from searching space
15:       $k^* = \underset{k}{\operatorname{argmin}} |\frac{k}{4m} - r|$ 
```

102 (GCD) of k and $4m$ are usually larger than 4 and do not fall in the three “good spatial coverage” cases in design rule 1. (3)
103 Integer frequency ratios r lead to worse trade-offs between fill-factor and scanning range. More discussions about this special
104 case is provided in the discussion section.

105 Modulated pattern design

We further consider a more challenging operation of resonant scanners: Regions-of-Interest (RoI) focusing. In a LiDAR system, through-put of the 3D sensor is fixed, which makes adaptive spatial sampling beneficial for various applications^{20,29,30}. More specifically, given a user-defined RoI, we aim at sampling the RoI as densely as possible in all frames. This type of scanning is particularly challenging for resonant scanners and is beyond the capability of the unmodulated scanning patterns, so we propose to use modulated scanning patterns. Such patterns contain multiple frequency components within the resonance bandwidth. However, due to the higher degrees-of-freedom and the complexity of user-defined RoI, analytical design rules are inadequate, so to design modulated scanning patterns, we develop an optimization-based approach. The framework is task-driven because different imaging tasks have different Regions-of-Interest (RoI) for spatial sampling. We seek to improve, by optimized modulation of the parameters, the operation of the resonant scanner as characterized by Equation 1. However, this model has continuous input parameters so we simplify the model through a Fourier expansion:

$$\begin{cases} x(t) = \sum_{n=n_1}^{n_2} \alpha_n H_x(\frac{n}{Lm}) \cos(2\pi \frac{n}{Lm} t) + \gamma_n H_x(\frac{n}{Lm}) \sin(2\pi \frac{n}{Lm} t), & \sqrt{\sum_n \alpha_n^2 + \gamma_n^2} \leq 1 \\ y(t) = \sum_{j=j_1}^{j_2} \beta_j H_y(\frac{j}{Lm}) \cos(2\pi \frac{j}{Lm} t) + \delta_j H_y(\frac{j}{Lm}) \sin(2\pi \frac{j}{Lm} t), & \sqrt{\sum_j \beta_j^2 + \delta_j^2} \leq 1 \end{cases} \quad (3)$$

106 where H_x and H_y are transfer function amplitudes. We ignore the phases of the transfer functions because they are included
107 in the coefficients of the cosine and sine terms. m specifies the frame time T_{frame} . n_1, n_2, k_1, k_2 defines the number of frequency
108 components in optimization. We find that generally, 5 frequency components give very good optimization results, and in most
109 cases, 3 frequency components are enough. L is an integer that controls the spacing of the frequency components. Note that
110 the amplitude constraints in Equation 3 are equivalent to bounding the root-mean-square (RMS) amplitudes of the actuation
111 signals. This is a looser constraint than bounding the absolute actuation amplitude in unmodulated scanning, which can be
112 expressed as $\sum_n \sqrt{\alpha_n^2 + \gamma_n^2} \leq 1, \sum_n \sqrt{\beta_n^2 + \delta_n^2} \leq 1$.

113 From Equation 3, we notice that the scanner motion is linearly determined by the parameter set $\{\alpha_n\}, \{\beta_k\}, \{\gamma_n\}, \{\delta_k\}$.
114 Also, due to the band-pass characteristics of the transfer functions H_x, H_y , only frequency components close enough to resonant
115 frequencies f_x^r, f_y^r have significant impact on scanner motion. This allows efficient optimization of the parameter set. We

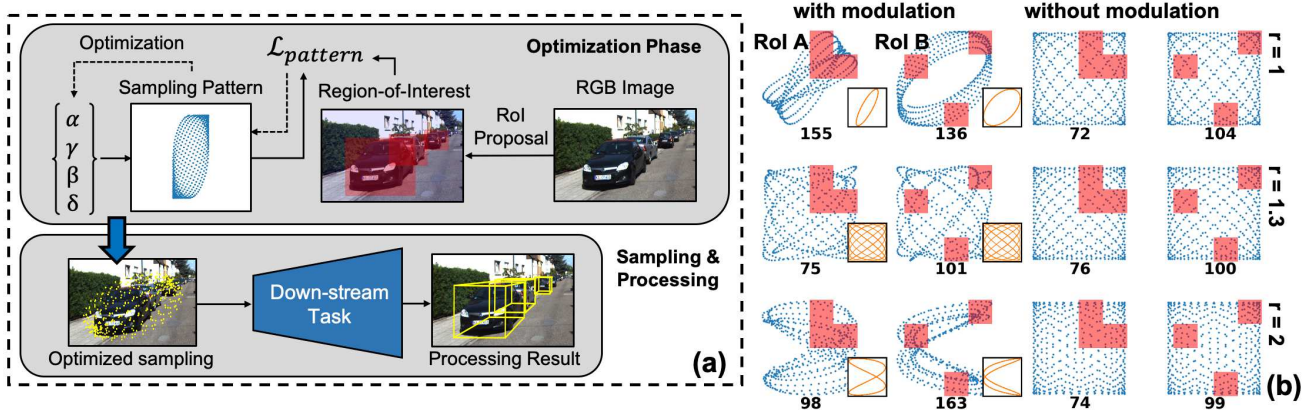


Figure 2. (a) Schematic pipeline of the proposed optimization framework. It shapes the sampling pattern into task-specific (or even scene-specific) RoI-focused patterns through objective function $\mathcal{L}_{pattern}$. Here 3D object detection is used as a target task. (b) Optimization results for different RoI and resonant frequency ratios. Red rectangles show the specified RoI and black numbers under each pattern show the amount of sampling points within the RoI. With $r \sim 1$ and $r \sim 2$, the modulated scanning patterns have denser sampling in RoI, compared to the reference unmodulated scanning patterns. However, with $r \sim 1.3$, this RoI focusing improvement is not significant. At the lower-right corner of each modulated pattern, we also show the corresponding basic unmodulated pattern.

116 further discretize time in Equation 3 to get the sampled scanning pattern $\mathbf{x} \in \mathbb{R}^N, \mathbf{y} \in \mathbb{R}^N$, where N is the number of sampling
 117 points. The resonant frequencies f_x^r, f_y^r , frame time T_{frame} and N are chosen as hyper-parameters in the optimization.

The optimization framework is shown in Figure 2(a). First, the parameter set is converted into a sampled scanning pattern \mathbf{x}, \mathbf{y} . For the specific task (in Figure 2(a), we use 3D object detection as an example), Regions-of-Interest (RoI) are proposed by a fast processing on 2D RGB image, or other heuristic rules and sensing results. The RoI is represented by a weight map \mathbf{W} and its values correspond to the importance of each regions in the FoV. With \mathbf{x}, \mathbf{y} and \mathbf{W} , we define the objective function $\mathcal{L}_{pattern}$ as:

$$\mathcal{L}_{pattern} = \sum_{i,j}^M \bar{W}_{i,j} [(x_i - \mathbf{x}[n_{i,j}])^2 + (y_j - \mathbf{y}[n_{i,j}])^2] \quad (4)$$

118 The $[-1, 1] \times [-1, 1]$ FoV (normalized by the product of amplitudes with on-resonance actuation) is divided into $M \times M$
 119 patches. For each patch (i, j) , we get the closest sampling point $(\mathbf{x}[n_{i,j}], \mathbf{y}[n_{i,j}])$ to its center location (x_i, y_j) and calculate the
 120 distance between these two points. $\bar{W}_{i,j}$ indicates the importance of each patch and is defined as the average weight in patch
 121 (i, j) . Patches with larger average weights have a higher priority during optimization. Note that if the distance between patch
 122 (i, j) and $(\mathbf{x}[n_{i,j}], \mathbf{y}[n_{i,j}])$ is smaller than a threshold, this patch is considered as occupied and $\bar{W}_{i,j}$ is set to zero, regardless the
 123 weight value in this patch. From $\mathcal{L}_{pattern}$, gradient decent optimization³¹ is performed on the parameter set $\{\alpha_n\}, \{\beta_k\}, \{\gamma_m\},$
 124 $\{\delta_k\}$. Once the optimization is done, spatial sampling can be conducted on a 3D scene, and a sparse point cloud is generated.
 125 The sampling is concentrated in the RoI, where most useful information is distributed, and the performance of down-stream
 126 tasks is improved. Note that this optimization need not to be done online (e.g. during scanner operation). For some tasks,
 127 optimized patterns for different scenes are very similar and thus the optimization process can be done off-line. An example is
 128 discussed in Supplementary Information.

129 Figure 2(b) shows optimization results for two randomly-selected RoI (RoI A, B) and different resonant frequency ratios.
 130 We use $T_{frame} = 7$, total sampling point number $N = 500$ in all optimizations. 5 frequency components are used in the
 131 optimization, with $f_x = \{6/7, 13/14, 1, 15/14, 8/7\}f_x^r, f_y = \{6/7, 13/14, 1, 15/14, 8/7\}f_y^r$. Similar results are achieved with
 132 3 frequency components $f_x = \{13/14, 1, 15/14\}f_x^r, f_y = \{13/14, 1, 15/14\}f_y^r$ and the effect of considering more frequency
 133 components (more than 5) within the range of $[6/7, 8/7]f_x^r, [6/7, 8/7]f_y^r$ is not significant. The first and the second columns
 134 show optimization results with modulated scanning patterns. The third and the fourth columns show reference unmodulated
 135 scanning patterns. The modulated scanning patterns have bounded RMS actuation amplitude, as defined in Equation 3, while
 136 the actuation amplitudes for unmodulated patterns are not bounded to better visualize the differences in RoI focused sampling.
 137 If the actuation amplitudes of unmodulated patterns are bounded, RoI on the edges and corners can't be reached in some cases.
 138 The comparisons show that: (1) With $r \sim 1, r \sim 2$, modulation and optimization lead to an improvement in sampling densities

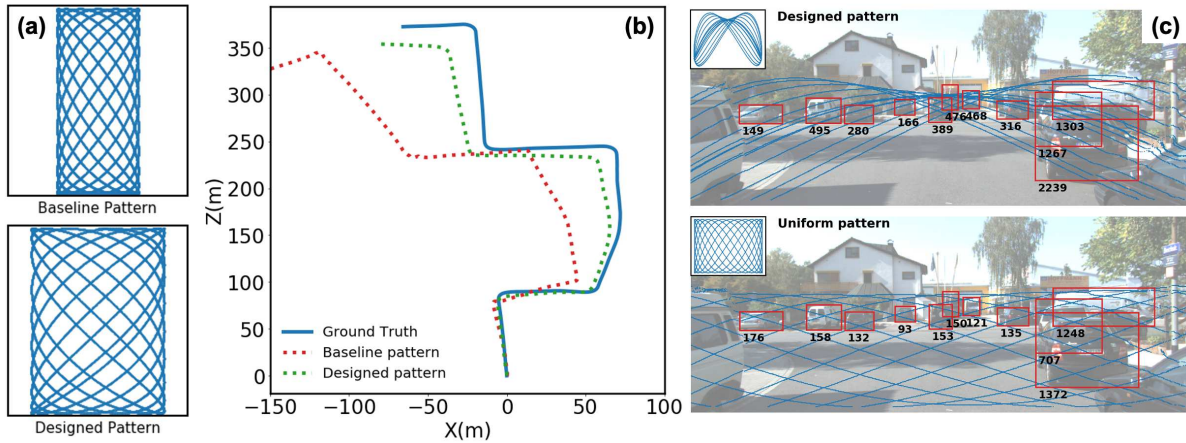


Figure 3. (a) Qualitative comparison of baseline and designed scanning patterns (P_1 and P_2 in Figure 1(a)). Scanning range of the designed pattern is $1.6\times$ of that in baseline pattern, leading to a larger perspective field and more reliable feature extraction. (b) Trajectory estimations with optimized scanning pattern and baseline scanning pattern. (c) Object detection with optimized pattern and baseline pattern. Each red bounding box contains an object and the black number at bottom indicates number of sampling points contained in the bounding box. Due to the RoI-focusing improvement, optimized pattern contains $\sim 3\times$ more sampling points in bounding boxes. The sampling patterns are shown in blue dots.

139 within the RoI, which are shown by the black number under each scanning pattern. (2) The RoI focusing improvement depends
 140 on the shape of the specified RoI. With $r \sim 1$, the RoI focusing is more successful for RoI A compared to RoI B, while it is
 141 the opposite with $r \sim 2$. (3) With $r \sim 1.3$, the RoI focusing improvement is very limited. The optimization results are only
 142 slightly improved compared to the unmodulated scanning patterns.

143 We provide a qualitative explanation for this dependence of RoI focusing improvement on resonant frequency ratio: A
 144 modulated scanning pattern “dithers” around a basic unmodulated scanning pattern, as shown in Figure 2(b) at the lower-right
 145 corner of each modulated pattern. This basic pattern corresponds to one pair of (f_x, f_y) in Equation 3 (it also needs to be in the
 146 resonance bandwidth). If the basic pattern has a short repeating period, it only traverse part of the scanning range. For example,
 147 with $f_x = 1, f_y = 1$, the scanning trajectory is a simple ellipse. Shape of the basic pattern is controlled by its amplitudes and
 148 phases in x and y-axis motion. When appropriate modulations are added, a small shift exists between the scanning trajectories
 149 in different repeating periods, and this leads to a focused sampling in the regions close to the basic pattern. However, if the
 150 basic pattern has a long repeating period and covers the scanning range uniformly, the modulated scanning patterns can’t be
 151 focused onto a certain portion of FoV through optimization. For $r \sim 1, r \sim 2$, the repeating period is very short with $f_x = f_y,$
 152 $f_x = 2f_y$. However, for $r \sim 1.3$, there does not exist a (f_x, f_y) pair close enough to resonance while also has a short repeating
 153 period (for example, shorter than $t = 2$).

154 Simulations

155 We evaluate the analytical design rule 1 and the proposed optimization framework in simulated 3D environments^{2,32}. Because
 156 most 3D imaging datasets currently available are acquired with a raster-scanned or a flash LiDAR, we develop a point cloud
 157 generation tool that generates a point cloud corresponding to a resonant scanning pattern. Details of the dataset, implementa-
 158 tion and more simulation results are provided in Supplementary Information.

159 LiDAR odometry with unmodulated scanning

160 LiDAR odometry algorithms estimate the trajectory of a moving agent during navigation. They extract feature points from a
 161 3D point cloud acquired in each frame. By comparing the spatial positions of these feature points between successive frames,
 162 the position of the agent in a world coordinate can be estimated.

163 In this work, we consider LiDAR odometry with resonant scanning patterns on the KITTI dataset². We adapt a Li-
 164 DAR odometry framework, named “LOAM”,^{3,33} into the resonant scanning scenario. For comparison, we use the example
 165 discussed in Figure 1(a) with pattern P_1 as the baseline and pattern P_2 as the designed pattern. As shown in Figure 3(a),
 166 Field-of-View (FoV) of P_2 is $\sim 1.6\times$ larger than that of P_1 . This much larger spatial region gives us more feature points to be
 167 observed and processed, which leads to more reliable trajectory estimation (for details of the extracted feature points, please

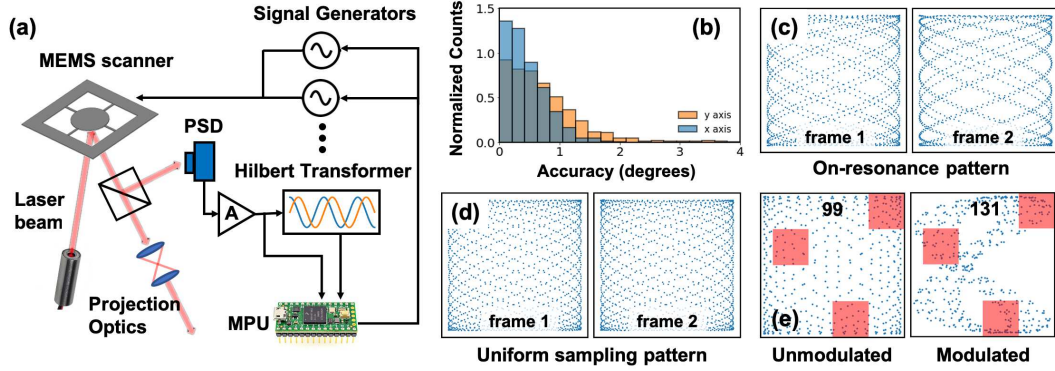


Figure 4. (a) Schematic of experimental set up for phase controlled resonant scanning. (b) Phase control accuracy of proposed hardware. (c) Recorded on-resonance scanning pattern, for two successive frames. (d) Recorded designed unmodulated sampling pattern, for two successive frames. (e) Recorded modulated sampling pattern with $r \sim 2.0$. Red rectangles are the Regions-of-Interest (RoI) and black numbers indicate amount of sampling points within RoI. Compared to the reference unmodulated scanning pattern, RoI sampling density is increased by $1.3\times$ with modulated scanning.

168 refer to Supplementary Information).

169 3D object detection with moduated scanning

170 Object detection is another task that is of great interest in 3D computer vision^{22,23}. The requirement it imposes on data
 171 collection is different from that in odometry. For each scene, important objects (e.g., cars, pedestrians) might concentrate
 172 in specific regions in the FoV. Therefore, a denser sampling in these Regions-of-Interest (RoI) is required. As an example,
 173 we use hyper-parameters $f_x^r = 1$, $f_y^r = 2$, $T_{frame} = 7$ and number of sampling points $N = 30000$. In Figure 3(c), we show
 174 the RoI-focused scanning pattern (upper row). The pattern consists of three frequency components ($f_x = \{\frac{13}{14}, 1, \frac{15}{14}\}$, $f_y =$
 175 $\{\frac{27}{14}, 2, \frac{29}{14}\}$). The relative phases and amplitudes of the three components are optimized to be ($\phi_x = \{86^\circ, 178^\circ, 86^\circ\}$, $\phi_y =$
 176 $\{-96^\circ, 145^\circ, -96^\circ\}$, $A_x = \{0.22, 0.95, 0.22\}$, $A_y = \{0.28, 0.91, 0.28\}$). Using more frequency components in this special case
 177 won't generate significant improvements. When compared to the sampling pattern designed for uniform sampling (lower row),
 178 the RoI-focused pattern samples significantly more points ($\sim 3\times$) in regions that contain important objects (cars in this scene).
 179 This will largely facilitate the object detection process²³. We do not conduct quantitative comparisons on object detection,
 180 due to the imperfectness in resonant-scanned point cloud generation. However, because of the positive relationship between
 181 sampling density and detection accuracy presented in previous literature^{2,23}, it is reasonable to expect an increase in accuracy
 182 when the optimized scanning pattern is used in real-world LiDAR system.

183 Note that in this task we do not follow the $f_x^r = r$, $f_y^r = 1$ setting. This is because the dataset we experiment on contains
 184 only road scenes. Such a scene is more likely to be symmetric in the horizontal direction compared to the vertical direction.
 185 For example, cars are more likely to be on the left and right sides of a road, instead of on the up and down sides of a road. As
 186 mentioned above, the performance of RoI focusing depends on the RoI shape. When the axis of symmetry of the RoI shape
 187 aligns with that of the scanning pattern, performance is improved. Therefore, we make the scanning pattern also symmetric in
 188 horizontal direction by choosing $f_x^r = 1.0$, $f_y^r = 2.0$ instead of $f_x^r = 2.0$, $f_y^r = 1.0$. Optimization results with $f_x^r = 2.0$, $f_y^r = 1.0$
 189 are also presented in Supplementary Information, where the performance is not as good as that in Figure 3, but still beats the
 190 reference unmodulated scanning pattern.

191 Experiments

192 We implement the designed scanning patterns (Figure 4(a)) using a MEMS scanner³⁴ with resonant frequencies $f_x^r = 2660\text{Hz}$,
 193 $f_y^r = 1100\text{Hz}$, i.e., a resonant frequency ratio $r = 2.42$. The quality factors for the two axis are $Q_x \sim 30$ and $Q_y \sim 50$. Because
 194 of the high Q factor and associated low bandwidth, we actuate the y-axis with a single frequency, and restrict modulation to the
 195 x-axis. A high-gain amplifier is used to maintain the scanning range when we operate at more than FWHM (Full Width at Half
 196 Maximum) away from the resonance. We developed a wide-band phase detection and control system to eliminate the inherent
 197 phase uncertainty in MEMS scanners. This uncertainty originates from the environmental sensitivity (e.g. to temperature) of
 198 MEMS devices and the strong dependence of the phase on deviations of the resonant frequency²⁵⁻²⁸. With the control system,
 199 we achieve $\sim 1^\circ$ phase control accuracy, as shown in Figure 4(b). To measure the accuracy, we detect the scanner phase

200 at beginning of each frame and compare it to the required phase, over 10 minutes of scanner operation. This calibration is
201 conducted with a high-speed oscilloscope not shown in Figure 4(a). The accuracy can be improved with faster MPU or better
202 position detection hardware. Phase stability with and without control are further discussed in the Supplementary Information.

203 Phase control in unmodulated scanning

204 We first demonstrate unmodulated scanning. During the experiments, the scanning patterns are recorded with a high-speed
205 position sensor (PSD). We choose $T_{frame} = 6.4ms$, corresponding to $T_{frame} = 7$ in design rule 1. Scanning patterns with
206 on-resonance actuation ($f_x = 2660$ Hz, $f_y = 1100$ Hz) and without phase control are shown in Figure 4(c), for two successive
207 frames. Most portions of the FoV are either over-sampled or under-sampled. Using our proposed design rule, the parameters
208 are changed to $f_x = 2672$ Hz, $f_y = 1100$ Hz, $\phi_x = \pi/14$ and $\phi_y = 0$. The corresponding scanning patterns have much higher
209 fill factor as shown in Figure 4(d).

210 Phase control in modulated scanning

211 To demonstrate modulated scanning, we drive the x-axis at three frequencies f_x , $13/14f_x$, $15/14f_x$ and drive the y-axis at a
212 single frequency f_y . Phases of the three components in the x-axis scanning are monitored and controlled at the beginning
213 of every 2 frames (when all three phases repeat). Resonant frequencies and frame time are set to be the same as that in the
214 unmodulated scanning experiment. As discussed above, with $r = 2.42$, ROI focusing improvement is limited. Therefore, we go
215 beyond the x-axis resonance bandwidth and select f_x actuation frequency components around 2200Hz while fix $f_y = 1100$ Hz
216 to emulate a MEMS scanner with $r = 2.0$. We focus the scanning pattern to ROI B in Figure 2(b) for demonstration. Due to
217 the high quality factor in y-axis, the degrees-of-freedom in optimization is reduced by $2\times$. However, ROI sampling density in
218 modulated scanning pattern still increases by $1.3\times$ compared to the unmodulated scanning pattern, as shown in Figure 4(e).
219 The experimentally acquired modulated sampling pattern is resampled to 500 sampling points per T_{frame} for comparison with
220 the sampling patterns in Figure 2.

221 Discussion

222 It is important to note how performance depends on resonant frequency ratios for unmodulated scanning design rule 1 and
223 modulated scanning. Different (f_x, f_y) pairs generate unmodulated scanning patterns with different repeating periods. For any
224 resonant frequency ratio r , pairs of (f_x, f_y) that correspond to long repeating period always exist in resonance bandwidth¹⁵.
225 However, a pair of (f_x, f_y) that corresponds to short repeating period might not exist, as in the case of $r \sim 1.3$. Also, a pair of
226 (f_x, f_y) that corresponds to repeating period $1/2T_{frame}$, T_{frame} or $2T_{frame}$ do not always exist, as in the case of $r \sim 1$, $r \sim 2$.
227 In the first situation, ROI focusing can't be achieved while in the second situation, uniform spatial sampling is difficult. In the
228 experiments, we noticed that ROI focusing performs efficiently only with $r \sim 1$ or $r \sim 2$ while these are the worst cases in
229 uniform spatial sampling, as shown in Figure 1. This result suggests the special usage for resonant scanners with resonance
230 frequency ratio $r \sim 1$, $r \sim 2$ in ROI focused sampling.

231 Although the proposed scanning pattern designs outperform the baselines, they have the following limitations. First,
232 both designs are based on a moderate quality factor Q . If the quality factor is too high, neither the frequency selection rule
233 in design rule 1 nor the modulated scanning pattern designs produce good results. Only small deviations from resonance
234 requires large actuation amplitudes, which is inconsistent with our bounded actuation setting. Second, the optimization
235 problem in modulated scanning pattern design is non-convex. Therefore, our approach does not guarantee convergence to
236 a global optimal. We also assume no cross-talk between x and y-axis scanner motions. This is consistent with the negligible
237 cross talk we observe in our MEMS scanners³⁴. If scanners with significant cross talk are employed, then the design rule for
238 unmodulated patterns have to be changed to give good results. ROI focusing, on the other hand, does not need substantial
239 changes to work with scanner that have cross talk. It is straightforward to contain the cross-talk in Equation 3 and use the
240 optimization framework for both uniform and ROI-focused spatial sampling design.

241 Conclusion

242 Spatial information acquisition is at the heart of many recent advances in the imaging and display industry. A fast and flexible
243 spatial sampling solution will largely improve the robustness and consumer experience. In this paper, we propose resonant
244 scanning pattern design and control schemes that improve the coverage, flexibility, and accuracy in fast spatial sampling. We
245 propose an analytical design rule for uniform spatial sampling, and an optimization-based framework for flexible, Regions-of-
246 Interest (ROI) focused spatial sampling. We also demonstrate the designed scanning patterns in an experimental prototype that
247 applies wide-band control on scanner motion. The proposed methods enable resonant-scanner LiDAR with a high frame-rate
248 ~ 100 Hz. When integrated with high-speed point cloud processing algorithms, such systems can be utilized in applications
249 across disciplines, including navigation, robotics, and augmented reality.

250 Methods

251 Phase control experimental setup

252 As shown in Figure 4(a), the MEMS scanner is actuated with signal generators (SIGLENT SDG2000X) controlled by external
253 phase modulation signals. The motion of MEMS is detected with a high-speed position sensor (ON-TRAK OT-301). This
254 motion signal is fed into an analog wide-band Hilbert transformer board for 90 degrees phase shift. Both motion signals $x(t)$,
255 $y(t)$ and the 90degrees phase shifted signals $\bar{x}(t)$, $\bar{y}(t)$ are sampled with an MPU chip (PJRC Teensy3.6). In practice, the
256 Hilbert transformer applies a frequency dependent phase shift on both output signals while the relative phase between these
257 two outputs is fixed to be $\pi/2$. We conduct calibrations to remove the phase offset and will ignore it in the following sections.
258 For more details, please refer to Supplementary Information. A fast processing algorithm is performed on the two signals to
259 get the phase and a feed-back signal is generated to the external modulation port of signal generators. Calibrations for each
260 components used in experiment are provided in Supplementary Information.

261 Phase calculation process

262 Phase calculations are simple for the unmodulated actuation case. After collecting $x(t)$ and $\bar{x}(t)$ at the beginning of each frame,
263 a fast arctangent calculation³⁵ is performed to get the phase. The detection process takes $\sim 15\mu s$.

For modulated actuation, phase detection and control is more complicated, because $x(t)$, $y(t)$ and $\bar{x}(t)$, $\bar{y}(t)$ contain multiple
frequency components. In this paper, we constrain ourselves to a comparatively simple situation: x axis actuation contains
three frequency components and y axis contains only single frequency component. Similar method can be extended to a more
general case. We express the scanner motion in the x -axis as:

$$\begin{cases} x(t) = \alpha_0 \cos(\omega_x^0 t + \phi_x^0) + \alpha_1 \cos(\omega_x^1 t + \phi_x^1) + \alpha_2 \cos(\omega_x^2 t + \phi_x^2) \\ \bar{x}(t) = \alpha_0 \sin(\omega_x^0 t + \phi_x^0) + \alpha_1 \sin(\omega_x^1 t + \phi_x^1) + \alpha_2 \sin(\omega_x^2 t + \phi_x^2) \end{cases} \quad (5)$$

There are three phases $\phi_x^i, i = 0, 1, 2$. We detect at both beginning of each frame and at the center of each frame to get six
equations:

$$\begin{cases} x(0) = \alpha_0 \cos(\phi_x^0) + \alpha_1 \cos(\phi_x^1) + \alpha_2 \cos(\phi_x^2), \\ x(T_{frame}/2) = \alpha_0 \cos(\omega_0 T_{frame}/2 + \phi_x^0) + \alpha_1 \cos(\omega_1 T_{frame}/2 + \phi_x^1) + \alpha_2 \cos(\omega_2 T_{frame}/2 + \phi_x^2), \\ x(T_{frame}) = \alpha_0 \cos(\omega_0 T_{frame} + \phi_x^0) + \alpha_1 \cos(\omega_1 T_{frame} + \phi_x^1) + \alpha_2 \cos(\omega_2 T_{frame} + \phi_x^2), \\ \bar{x}(0) = \alpha_0 \sin(\phi_x^0) + \alpha_1 \sin(\phi_x^1) + \alpha_2 \sin(\phi_x^2), \\ \bar{x}(T_{frame}/2) = \alpha_0 \sin(\omega_0 T_{frame}/2 + \phi_x^0) + \alpha_1 \sin(\omega_1 T_{frame}/2 + \phi_x^1) + \alpha_2 \sin(\omega_2 T_{frame}/2 + \phi_x^2), \\ \bar{x}(T_{frame}) = \alpha_0 \sin(\omega_0 T_{frame} + \phi_x^0) + \alpha_1 \sin(\omega_1 T_{frame} + \phi_x^1) + \alpha_2 \sin(\omega_2 T_{frame} + \phi_x^2), \end{cases} \quad (6)$$

264 Equation 6 is linear in $\{\alpha_i \cos(\phi_x^i), \alpha_i \sin(\phi_x^i)\}, i = 1, 2, 3$, a fast matrix multiplication is used to solve them. Then we apply
265 the fast arctangent calculation on each (\cos, \sin) pair separately to get the phases. The whole data acquisition and processing
266 takes $\sim 40\mu s$ for three frequency components.

267 References

- 268 1. Cadena, C., Dick, A. R. & Reid, I. D. Multi-modal auto-encoders as joint estimators for robotics scene understanding. In
269 *Robotics: Science and Systems*, vol. 5, 1 (2016).
- 270 2. Geiger, A., Lenz, P., Stiller, C. & Urtasun, R. Vision meets robotics: The kitti dataset. *The Int. J. Robotics Res.* **32**,
271 1231–1237 (2013).
- 272 3. Zhang, J. & Singh, S. Loam: Lidar odometry and mapping in real-time. In *Robotics: Science and Systems*, vol. 2 (2014).
- 273 4. Yoo, H. W. *et al.* MemS-based lidar for autonomous driving. *e & i Elektrotechnik und Informationstechnik* **135**, 408–415
274 (2018).
- 275 5. Henry, P., Krainin, M., Herbst, E., Ren, X. & Fox, D. Rgb-d mapping: Using kinect-style depth cameras for dense 3d
276 modeling of indoor environments. *The Int. J. Robotics Res.* **31**, 647–663 (2012).
- 277 6. Loewke, N. O. *et al.* Software-based phase control, video-rate imaging, and real-time mosaicing with a lissajous-scanned
278 confocal microscope. *IEEE Transactions on Med. Imaging* **39**, 1127–1137 (2019).
- 279 7. Wu, T., Ding, Z., Wang, K., Chen, M. & Wang, C. Two-dimensional scanning realized by an asymmetry fiber cantilever
280 driven by single piezo bender actuator for optical coherence tomography. *Opt. express* **17**, 13819–13829 (2009).
- 281 8. Zhang, C., You, Z., Huang, H. & Li, G. Study on a two-dimensional scanning micro-mirror and its application in a moems
282 target detector. *Sensors* **10**, 6848–6860 (2010).

- 283 **9.** Newman, J. A. *et al.* Multi-channel beam-scanning imaging at khz frame rates by lissajous trajectory microscopy. In
284 *Three-Dimensional and Multidimensional Microscopy: Image Acquisition and Processing XXII*, vol. 9330, 933009 (Inter-
285 national Society for Optics and Photonics, 2015).
- 286 **10.** Sullivan, S. Z. *et al.* High frame-rate multichannel beam-scanning microscopy based on lissajous trajectories. *Opt. express*
287 **22**, 24224–24234 (2014).
- 288 **11.** Tuma, T., Lygeros, J., Kartik, V., Sebastian, A. & Pantazi, A. High-speed multiresolution scanning probe microscopy
289 based on lissajous scan trajectories. *Nanotechnology* **23**, 185501 (2012).
- 290 **12.** Milanovic, V., Castelino, K. & McCormick, D. T. Highly adaptable mems-based display with wide projection angle. In
291 *2007 IEEE 20th International Conference on Micro Electro Mechanical Systems (MEMS)*, 143–146 (IEEE, 2007).
- 292 **13.** Ashida, Y., Hamann, S., Landry, J. & Solgaard, O. Conjugated mems phased arrays for large field of view random access
293 scanning. *IEEE Photonics Technol. Lett.* **32**, 1291–1294 (2020).
- 294 **14.** Hamann, S., Ceballos, A., Landry, J. & Solgaard, O. High-speed random access optical scanning using a linear mems
295 phased array. *Opt. letters* **43**, 5455–5458 (2018).
- 296 **15.** Hwang, K., Seo, Y.-H., Ahn, J., Kim, P. & Jeong, K.-H. Frequency selection rule for high definition and high frame rate
297 lissajous scanning. *Sci. reports* **7**, 1–8 (2017).
- 298 **16.** Seo, Y.-H., Hwang, K., Kim, H. & Jeong, K.-H. Scanning mems mirror for high definition and high frame rate lissajous
299 patterns. *Micromachines* **10**, 67 (2019).
- 300 **17.** Tuma, T., Lygeros, J., Sebastian, A. & Pantazi, A. Optimal scan trajectories for high-speed scanning probe microscopy.
301 In *2012 American Control Conference (ACC)*, 3791–3796 (IEEE, 2012).
- 302 **18.** Wang, J., Zhang, G. & You, Z. Design rules for dense and rapid lissajous scanning. *Microsystems & Nanoeng.* **6**, 1–7
303 (2020).
- 304 **19.** Wu, J.-W., Lin, Y.-T., Lo, Y.-T., Liu, W.-C. & Fu, L.-C. Lissajous hierarchical local scanning to increase the speed of
305 atomic force microscopy. *IEEE Transactions on Nanotechnol.* **14**, 810–819 (2015).
- 306 **20.** Bergman, A. W., Lindell, D. B. & Wetzstein, G. Deep adaptive lidar: End-to-end optimization of sampling and depth
307 completion at low sampling rates. In *2020 IEEE International Conference on Computational Photography (ICCP)*, 1–11
308 (IEEE, 2020).
- 309 **21.** Li, Q. *et al.* Lo-net: Deep real-time lidar odometry. In *Proceedings of the IEEE Conference on Computer Vision and*
310 *Pattern Recognition*, 8473–8482 (2019).
- 311 **22.** Qi, C. R., Su, H., Mo, K. & Guibas, L. J. Pointnet: Deep learning on point sets for 3d classification and segmentation. In
312 *Proceedings of the IEEE conference on computer vision and pattern recognition*, 652–660 (2017).
- 313 **23.** Qi, C. R., Liu, W., Wu, C., Su, H. & Guibas, L. J. Frustum pointnets for 3d object detection from rgb-d data. In
314 *Proceedings of the IEEE conference on computer vision and pattern recognition*, 918–927 (2018).
- 315 **24.** Doshi, N., Jayaram, K., Goldberg, B. & Wood, R. J. Phase control for a legged microrobot operating at resonance. In
316 *2017 IEEE International Conference on Robotics and Automation (ICRA)*, 5969–5975 (IEEE, 2017).
- 317 **25.** Csencsics, E. & Schitter, G. Design of a phase-locked-loop-based control scheme for lissajous-trajectory scanning of fast
318 steering mirrors. In *2017 American Control Conference (ACC)*, 1568–1573 (IEEE, 2017).
- 319 **26.** Csencsics, E. & Schitter, G. System design and control of a resonant fast steering mirror for lissajous-based scanning.
320 *IEEE/ASME Transactions on Mechatronics* **22**, 1963–1972 (2017).
- 321 **27.** Manosalvas-Kjono, S., Quan, R. & Solgaard, O. Method and apparatus for evaluating electrostatic or nonlinear devices
322 (2019). US Patent App. 16/270,374.
- 323 **28.** Csencsics, E., Saathof, R. & Schitter, G. Design of a dual-tone controller for lissajous-based scanning of fast steering
324 mirrors. In *2016 American Control Conference (ACC)*, 461–466 (IEEE, 2016).
- 325 **29.** Betterton, J.-R., Ratner, D., Webb, S. & Kochenderfer, M. Reinforcement learning for adaptive illumination with x-rays.
326 In *2020 IEEE International Conference on Robotics and Automation (ICRA)*, 328–334 (IEEE, 2020).
- 327 **30.** Godaliyadda, G. D. P. *et al.* A framework for dynamic image sampling based on supervised learning. *IEEE Transactions*
328 *on Comput. Imaging* **4**, 1–16 (2017).
- 329 **31.** Ruder, S. An overview of gradient descent optimization algorithms. *arXiv preprint arXiv:1609.04747* (2016).

- 330 **32.** Silberman, N., Hoiem, D., Kohli, P. & Fergus, R. Indoor segmentation and support inference from rgbd images. In
331 *European conference on computer vision*, 746–760 (Springer, 2012).
- 332 **33.** Lin, J. & Zhang, F. Loam livox: A fast, robust, high-precision lidar odometry and mapping package for lidars of small
333 fov. In *2020 IEEE International Conference on Robotics and Automation (ICRA)*, 3126–3131 (IEEE, 2020).
- 334 **34.** Jeong, J.-W., Kim, S. & Solgaard, O. Split-frame gimbaled two-dimensional mems scanner for miniature dual-axis
335 confocal microendoscopes fabricated by front-side processing. *J. microelectromechanical systems* **21**, 308–315 (2011).
- 336 **35.** Rajan, S., Wang, S., Inkol, R. & Joyal, A. Efficient approximations for the arctangent function. *IEEE Signal Process.*
337 *Mag.* **23**, 108–111 (2006).
- 338 **36.** Ma, F., Cavalheiro, G. V. & Karaman, S. Self-supervised sparse-to-dense: Self-supervised depth completion from lidar
339 and monocular camera. In *2019 International Conference on Robotics and Automation (ICRA)*, 3288–3295 (IEEE, 2019).
- 340 **37.** Barron, J. T. & Poole, B. The fast bilateral solver. In *European Conference on Computer Vision*, 617–632 (Springer,
341 2016).
- 342 **38.** Alhashim, I. & Wonka, P. High quality monocular depth estimation via transfer learning. *arXiv preprint arXiv:1812.11941*
343 (2018).
- 344 **39.** https://labcit.ligo.caltech.edu/~ajw/ph106/Files_ph106a/ph106a_2019_L7.pdf.
- 345 **40.** Weng, X. & Kitani, K. A baseline for 3d multi-object tracking. *arXiv preprint arXiv:1907.03961* **1**, 6 (2019).
- 346 **41.** Chiu, H.-k., Prioletti, A., Li, J. & Bohg, J. Probabilistic 3d multi-object tracking for autonomous driving. *arXiv preprint*
347 *arXiv:2001.05673* (2020).

348 **Author contributions statement**

349 Z. Sun conducted the simulation and experimental work. R. Quan conducted circuit design and provided critical suggestions.
350 O. Solgaard supervised the project. All authors reviewed the manuscript.

351 **Competing interests**

352 The author(s) declare no competing interests.

353 **Data availability**

354 All data used in plotting the figures (including figures in Supplementary Information) are available at
355 https://drive.google.com/drive/folders/1I5_auWKR-UVEHSugAnWArbaphlW4iKL?usp=sharing

Supplementary Information

Unmodulated scanning pattern design

Concepts of “repeating pattern” and “frame time”

We note that the terms “repeating pattern” and “frame time” are used in previous literature^{9,10} while their definitions are different from those used in this paper. To avoid confusion, here we give a detailed comparison between the concepts:

In previous literature^{9,10}, a “non-repeating pattern” is defined as a resonant scanning pattern with irrational scanning frequency ratio and never repeats. Any scanning pattern that repeats in limited time is denoted as a “repeating pattern”. Accordingly, the “frame time” is defined as the repeating period of a resonant scanning pattern.

In this paper, we focus on optimization of scanning pattern in a short, given time T_{frame} . We denote T_{frame} as “frame time”, while it does not necessarily equal the repeating period of scanning pattern. The “frame” here refers to a time period in which one block of data is collected. This data block is processed individually and is not combined with data from other “frames”. The “frame time” is a manually given input in the proposed design rule. Practically, it can be the safety response time of an autonomous vehicle and is specified by a higher-level system requirement. The concurrent research¹⁸ shared similar concepts with us. However, they only considered scanning patterns that repeat in each “frame time” (denoted as “repeating pattern” in this paper) and ignore the physical constraint of maximum actuation amplitude in their design. The proposed design rule expands the design space to include patterns that does not repeat in each “frame time” (denoted as “non-repeating pattern” in this paper). Therefore, it is more complete and achieves better performance.

Derivation of unmodulated scanning pattern design rule

The intuitive starting point of proposed unmodulated scanning pattern design rule is:

The scanning trajectory can't repeat (or almost repeat) itself at middle of a frame.

As long as this criteria is met, the scanning pattern within $T_{frame} = m$ has a good fill-factor. Without loss of generality, we make the same assumption as in the main text (since we focus on unmodulated scanning pattern design in this subsection, we ignore the time-dependence of amplitudes A_x, A_y and phases ϕ_x, ϕ_y):

$$\begin{cases} x(t) = A_x \cos(2\pi f_x t + \phi_x), & p_x(t) \equiv 2\pi f_x t + \phi_x \\ y(t) = A_y \cos(2\pi f_y t + \phi_y), & p_y(t) \equiv 2\pi f_y t + \phi_y \\ f_x = p/q, & p, q \text{ coprime} \\ f_y = 1, & \phi_y = 0 \end{cases} \quad (7)$$

Where f_x, f_y, ϕ_x, ϕ_y are the frequencies and phases for two scanning axis. We define two new variables, $p_x(t), p_y(t)$ as the instance phases, for simplicity. We define a set of t such that $\text{mod}[p_y(t), \pi] = 0$. We denote this set of t as T_{nodes} . With the above assumptions, $T_{nodes} = \{n/2\}, n \in \mathbb{Z}$. When $\text{mod}[p_y(t), \pi] = 0$ and $\text{mod}[p_x(t), \pi] = 0$ both hold, the scanning trajectory begins to repeat itself. If t does not coincide with the beginning or end of a frame, the fill-factor of scanning pattern reduces significantly. Also, with $t \in T_{nodes}$, if $|\text{mod}[p_x(t), \pi]|$ is small, the scanning pattern also follows a trajectory that is close to self-repeating. To provide an optimal scanning pattern, we want $|\text{mod}[p_x(t), \pi]|$ to be as large as possible for $\forall t \in T_{nodes}$, except when t is at the beginning or end of a frame. Starting from this observation, we list several conclusions that leads to the three cases in design rule 1:

- First, repeating period of the scanning pattern (equals to q) must be synchronized with the frames. That is, $q = km, k \in \mathbb{Z}^+$. Otherwise, no matter how phases are chosen, the scanning pattern repeats its trajectory at least within some frames. This does not meet the criteria.
- **With $q = m$, which corresponds to Case3 in design rule 1**, selecting the phase ϕ_x is important. With $t \in T_{nodes} = \{n/2\}, n \in \mathbb{Z}$, $\rightarrow p_x(t) = np\pi/m + \phi_x$. Since p, m coprime, $p_x(t)$ value traverses the set $\{k\pi/m + \phi_x\}, k \in \{0, 1, 2, \dots, m-1\}$. Therefore, the minimum value of $|\text{mod}[p_x(t), \pi]|$ is either $|\phi_x - \pi/m|$ or ϕ_x . If either one of these two values is small, the pattern is close to self-repeating. To make both values sufficiently large, we choose $\phi_x = \pi/(2m)$, such that $|\phi_x - \pi/m|$ also equals to $\pi/(2m)$.
- **$q = 2m$ corresponds to Case2 in design rule 1**. Similar to the above derivations, with $t = n/2, n \in \{0, 1, 2, \dots, 2m-1\}$, the minimum value of $|\text{mod}[p_x(t), \pi]|, t \in T_{nodes}$ is either $|\phi_x - \pi/(2m)|$ or ϕ_x . Therefore, we choose $\phi_x = 0$, such that the minimum value of $|\text{mod}[p_x(t), \pi]|$ is only achieved at $t = 0$, the beginning of a frame.
- **$q > 2m$** , similar to the above derivations, with $t = n/2, n \in \{0, 1, 2, \dots, 2m-1\}$, the minimum value of $|\text{mod}[p_x(t), \pi]|, t \in T_{nodes}$ is either $|\phi_x - \pi/q|$ or ϕ_x . No matter how we choose ϕ_x , the minimum value of $|\text{mod}[p_x(t), \pi]|$ won't be larger than π/q . Since $q > 2m$, usually fill-factor of the scanning pattern reduces significantly.

- **Heuristically, we find an exception with $q = 4m$, which corresponds to Case1 in design rule 1.** Although the minimum value of $|\text{mod}[p_x(t), \pi]|, t \in T_{nodes}$ equals to $\pi/(4m)$, it only happens once and at any other $t \in T_{nodes}$, $|\text{mod}[p_x(t), \pi]| \geq \pi/(2m)$. If $|\text{mod}[p_x(t), \pi]| = \pi/(4m)$ only happens close to beginning or end of frames, the fill-factor reduction can be ignored, as in the example discussed in main text (Figure 1(a), Pattern 2). Therefore, we add an additional check for Case1:

$$\forall t \in T_{nodes}, |\text{mod}[t, m]| > [m/2], \text{ (These } t \text{ values are not close enough to beginning or end of frames),} \quad (8)$$

$$|\text{mod}[p_x(t), \pi]| \neq \pi/(4m)$$

- **We also give an explanation on why $q = 3m$ and $q = 5m$ are not selected.** Similar to Case3, when $q = 3m$, the minimum value of $|\text{mod}[p_x(t), \pi]|, t \in T_{nodes}$ equals to $\pi/(3m)$. It only happens once and at any other $t \in T_{nodes}$, $|\text{mod}[p_x(t), \pi]| \geq 2\pi/(3m)$. If $|\text{mod}[p_x(t), \pi]| = \pi/(3m)$ only happens close to beginning or end of frames, the fill-factor reduction should be tolerable. However, suppose $t_1 \in T_{nodes}$, $|\text{mod}[p_x(t_1), \pi]| = \pi/(3m)$, we have $t_1 + 3m/2 \in T_{nodes}$, $|\text{mod}[p_x(t_1 + 3m/2), \pi]| = |\text{mod}[p_x(t_1) + p\pi, \pi]| = \pi/(3m)$. The separation between t_1 and $t_1 + 3m/2$ is $3/2$ of a frame time m . Therefore, it is impossible for both t_1 and $t_1 + 3m/2$ to be close to beginning or end of frames, which means there are always some frames with low fill-factor.

Similar explanation is valid for $q = 5m$.

- With $q \geq 6m$, the fill-factor reduction is worse than the case $q = 4m$. This is because even if the minimum value of $|\text{mod}[p_x(t), \pi]|$ is achieved close to beginning or end of frames, part of the k th minimum values, $k \geq 2$ are also small enough to significantly influence the fill-factor. **Therefore, we do not include the cases with $q > 4m$ in design rule 1.**

Fill-factor computation for unmodulated scanning patterns

To quantitatively calculate the fill-factor for a scanning pattern, we first scale a scanning pattern into $[-1, 1] \times [-1, 1]$ range, because fill-factor should not depend on scanning range (size of scanning pattern). Then we sample 1000 points from this scaled pattern, with equal time interval. We divide the $[-1, 1] \times [-1, 1]$ range into 128×128 patches. For each patch, we search for a minimum distance from its center to the set of sampling points. Finally, we take the maximum value among these minimum distances as R_{max} , radius of the largest inscribed circle.

Phase error tolerance in unmodulated scanning pattern designs

Small uncertainties in phases are unavoidable in real-world system, even with well-designed controls. Here we analyze the phase tolerance of the proposed unmodulated scanning design rule. In Figure 5, we plot the fill-factor vs. resonant frequency ratio $r \in [1, 3]$, with a small phase shift $\delta\phi_x$ added to the designed phase ϕ_x . As can be seen, with $\delta\phi_x$, sampling efficiency significantly reduces, but is still at a reasonable value. Also, we noticed that the degradation in sampling efficiency does not grow with the phase error. This is due to the periodic nature of resonant scanning patterns.

Simulation details

We will provide all scripts used in simulations on publication:

<https://github.com/zhsun0357/Resonant-Scanned-LiDAR>

Dataset generation

We generate the resonant-scanned point cloud from KITTI dataset² and NYUV2 dataset³² for scanning pattern evaluations. For KITTI dataset, we first generate a dense depth map with depth inpainting algorithm³⁶. We interpret \mathbf{x}, \mathbf{y} in sampling pattern as the normalized yaw angle ϕ and pitch angle θ . With the calibrated transformation matrix between camera coordinate and LiDAR coordinate, we are able to sample a 3D point cloud in LiDAR coordinate from the dense depth map with ϕ and θ . There are two major limitations in this point cloud generation process. First, we crop the 360° scanned point cloud in KITTI dataset into an horizontal angle (yaw angle ϕ) range $\sim \pm 40^\circ$, corresponding to the camera FoV. This is because we need the RGB image as reference in depth inpainting³⁶ while naive depth inpainting without reference RGB image results in large error. Second, due to the pixelization and imperfect estimation in the dense depth map, the resulted resonant-scanned point cloud is geometrically distorted compared to raw point cloud from KITTI dataset. An example of the generated point cloud from KITTI dataset is shown in Figure 6(a), in bird's-eye view. We crop out a local patch in the generated point cloud and compare it to the corresponding reference point cloud from raster-scanned, raw KITTI data. Although the surfaces (e.g., buildings, cars) are generally maintained, small geometric errors can be noticed. This distortion leads to difficulties when implementing object detection on sampled point cloud, because detection results on resonant-scanned point cloud can't be compared with ground truth for raw point cloud. Therefore, we do not show the quantitative comparison on object detection accuracy in the paper.

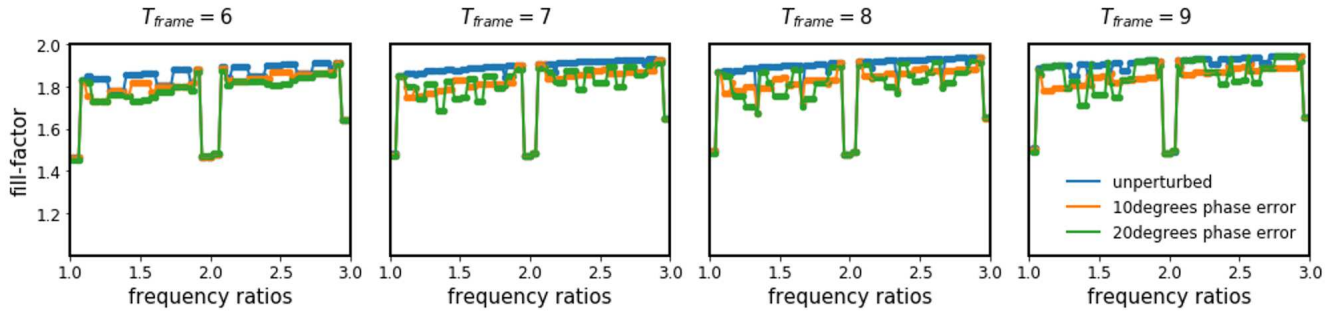


Figure 5. Analysis on phase error tolerance in the unmodulated scanning pattern design. A phase error of $10^\circ/20^\circ$ are added to ϕ_x when generating the scanning pattern. Compared to the non-perturbed patterns, this phase error results in a degradation in sampling efficiency.

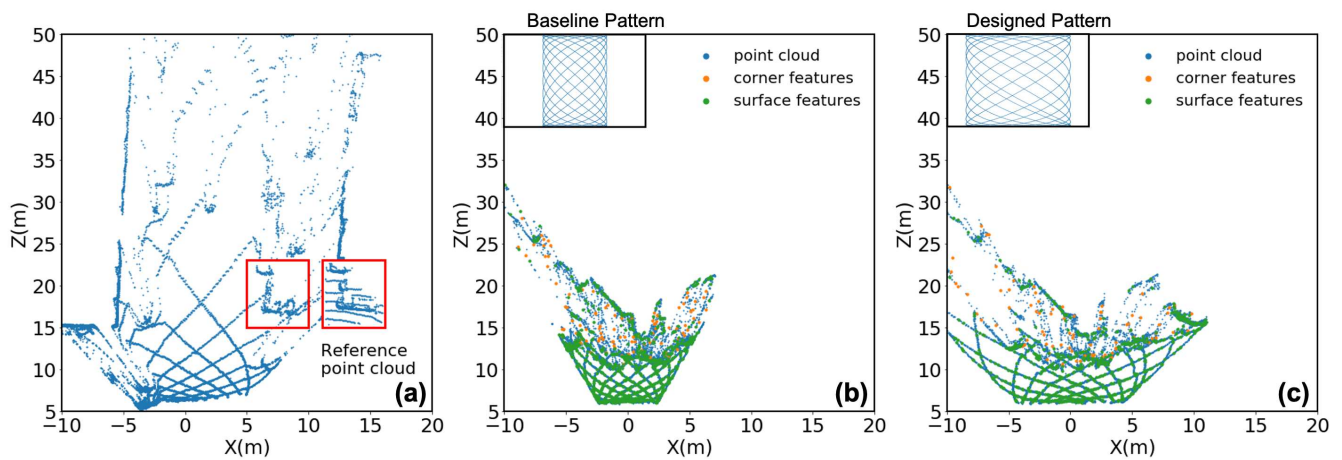


Figure 6. (a) An example generated resonant-scanned point cloud (in bird's-eye view). Note the distortions compared to corresponding raster-scanned "reference point cloud" in KITTI dataset. (b)(c) Feature points extraction (for both surface and corner features) with baseline/optimized sampling patterns in bird's-eye view. Blue points correspond to the full point cloud, orange and green points correspond to corner and surface feature points separately.

438 Nevertheless, through the proposed task-driven optimization, enhancement in sampling density in the Regions-of-Interest is
 439 evident. Due to the positive relationship between sampling density and detection accuracy presented in previous literature^{2,23},
 440 it is reasonable to expect an increase in accuracy when the optimized scanning pattern is used in real-world LiDAR system.
 441 For NYUV2 dataset, since a dense depth map is provided, straight-forward sampling on this dense depth map is conducted.
 442 Sampling pattern x and y are directly converted into pixel coordinates in the dense depth map.

443 Implementation

444 For LiDAR odometry task, we adapt the framework "LOAM" from previous literature³. The trajectory estimation process
 445 can be divided into three steps: 1. Divide LiDAR point cloud into multiple scan sections 2. Corner/Surface feature extraction
 446 from each section and 3. Trajectory estimation with the extracted features. To better estimate the quality of data collected in
 447 a single frame, we do not contain a global mapping step in the algorithm. In Figure 6(b)(c), we show extracted feature points
 448 with baseline and designed patterns. Two types of feature points are extracted: corner features that provide in-line geometric
 449 constraints and surface features that provide in-plane constraints. A larger Field-of-view (FoV) of designed pattern contains
 450 more high-quality feature points and thus makes the odometry estimation more reliable.

451 Apart from the example of scanning pattern optimization in object detection (shown in main text), we demonstrate the
 452 mechanism of the proposed optimization framework with another computer vision task: depth inpainting. Depth inpainting
 453 involves generating a dense depth map from a sparsely sampled point cloud (and optionally, a reference RGB image). In this
 454 work, we adapt a state-of-the-art depth inpainting framework²⁰ for task-driven scanning pattern optimization. We use multiple

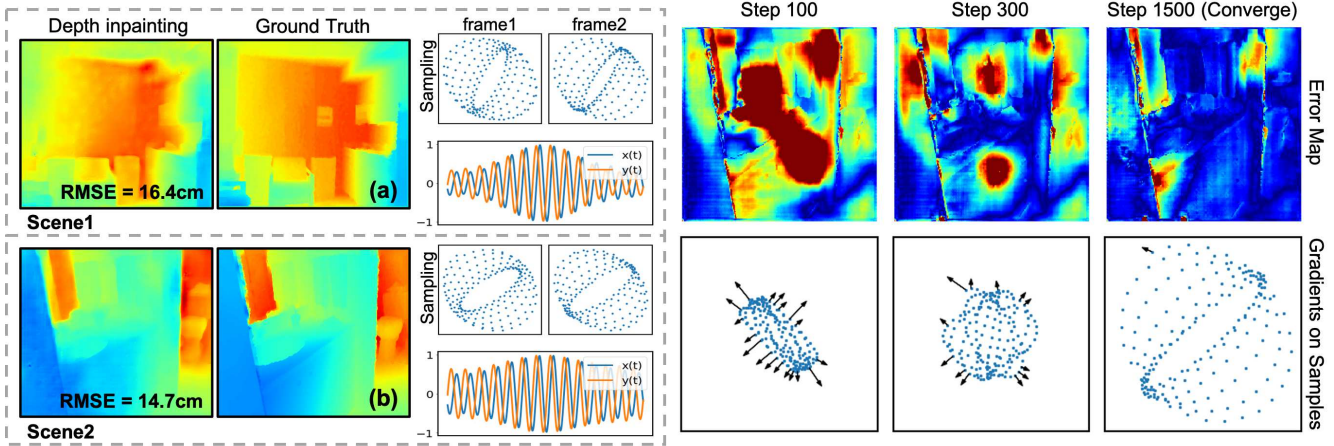


Figure 7. (a), (b) For two scenes in NYUV2 dataset, we show the optimized sampling pattern with $N = 200$ sampling points. We also show the modulated $x(t)$, $y(t)$ with optimized parameter set. On the left part of (a), (b), depth inpainting results with optimal sampling patterns are compared with ground truth depth map. Root-mean-square-errors (RMSE) are listed for each scene. (c) Weight (error) map and gradients on sampling pattern at different optimization steps. Amplitudes and signs of gradients are indicated by the lengths and directions of black arrows.

455 scenes in NYUV2 dataset³² to get optimized scanning patterns. Regions-of-Interest weight is estimated by the relative absolute
 456 error at each pixel during training. Hyper-parameters $f_x^r = 1$, $f_y^r = 1$, $T_{frame} = 7$ and number of sampling points $N = 200$ are
 457 used.

458 As shown in Figure 7(a),(b), it turns out that optimizations with different scenes in the dataset converge to very similar
 459 optimal scanning patterns. This is due to the fact that in depth inpainting, each position in the whole FoV is of almost
 460 equivalent importance. Therefore, instead of an RoI-focused sampling, a better design for this task might be directly using
 461 the unmodulated design. As mentioned in the scanner motion model, in task-driven optimization, the constraint on actuation
 462 amplitude is loosened. For the example shown in Figure 7, optimized scanning pattern requires peak actuation amplitude
 463 ~ 2.0 . To get comparable performance, unmodulated scanning pattern only requires an actuation signal with peak amplitude
 464 ~ 1.3 .

465 The depth inpainting framework proposed by Bergman et al.²⁰ consists of a rough bilateral filter stage³⁷ and a refinement
 466 stage. The model also contains a monocular depth estimator³⁸ to assist the inpainting task. The whole inpainting algorithm is
 467 accomplished by an end-to-end convolutional neural network (CNN), where the bilateral filter is also approximated by an CNN
 468 model. Instead of that, we use the original bilateral filter in the pipeline, and directly use the error-map from this bilateral filter
 469 stage for optimization. The advantage of the proposed optimization framework, compared with that in previous literature²⁰ is:
 470 RoI information across the whole FoV has impact on the scanning pattern updating, even when the non-optimized sampling
 471 region is small. Examples of the gradients on sampling pattern at different optimization steps are shown in Figure 7. It can be
 472 seen that at each step, gradients on sampling points are “stretching” the sampling pattern to uncovered regions. Note that in an
 473 early step (step 100), the inpainting result is rough and RoI-weight (error) is even larger in the sampled region. This might be
 474 due to the fact that depth reconstruction in these initially sampled regions is coincidentally more difficult. However, occupied
 475 patches are set with zero weights in objective function. Therefore, despite this RoI-weight distribution, the optimization
 476 framework still managed to “expand” the sampling pattern instead of “trapping” it in a local region with large error.

477 We also show the RoI focusing optimization result for 3D object detection with $f_x = 2.0$, $f_y = 1.0$ in Figure 8. Although the
 478 axis of symmetry of the scene does not align with that of the scanning pattern, modulated scanning pattern still out-performs
 479 the reference unmodulated scanning pattern significantly.

480 Considerations in dynamic scenes

481 In the main text, we focus on optimizing scanning pattern in each data collection period T_{frame} and assume a static environ-
 482 nment. In real-world LiDAR applications, adjusting scanning pattern design according to dynamic scenes is also an important
 483 functionality. Here we briefly analyze how to adapt the proposed designs to this scenario.

484 In unmodulated scanning pattern design, the goal is an optimal uniform spatial sampling. With a fixed resonant frequency
 485 ratio r and a fixed frame time T_{frame} , the optimal scanning pattern is uniquely given by design rule 1 and is not related to the

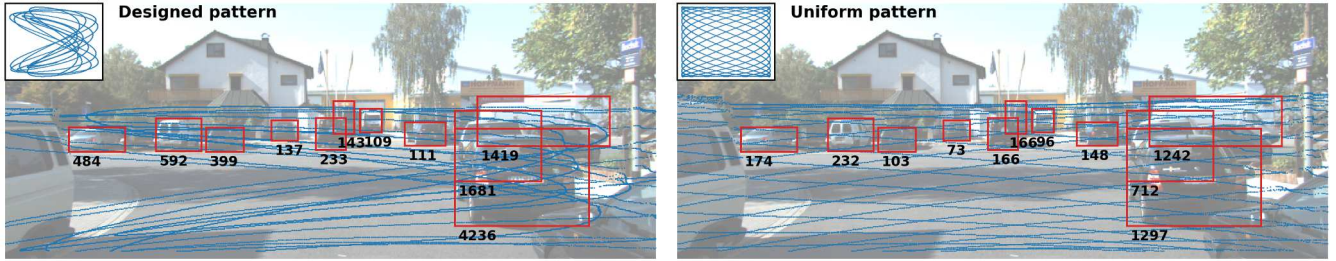


Figure 8. RoI focusing optimization result for 3D object detection with $f_x = 2.0$, $f_y = 1.0$.

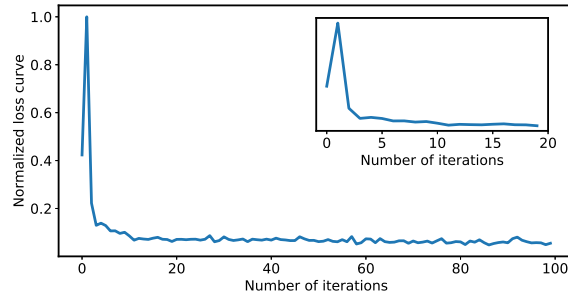


Figure 9. A typical convergence curve in the modulated scanning pattern optimization. The inset is a zoom-in view for iteration steps less than 20. Usually partial convergence is achieved within 10 to 20 iteration steps. With better initialization strategy, the convergence steps can be reduced to < 5 (not shown in the figure)

486 scene. The designed unmodulated scanning patterns repeat (Case2,3 in design rule 1) or almost repeat (Case1 in design rule
 487 1) in each T_{frame} , regardless the changes in the scene. This is the same case as in most LiDAR systems and we demonstrate
 488 its effectiveness in the LiDAR odometry task.

489 In modulated scanning pattern design, the goal is RoI-focusing and in many cases, the optimized scanning pattern is
 490 preferred to change with the scene. When the RoI changes, to make the transition from a previously designed scanning pattern
 491 to an updated one, time delay is inevitable. In the proposed scanning pattern design and control framework, this time delay
 492 majorly consists of MEMS device response time and scanning pattern design computation time. The MEMS response time is
 493 roughly given by $t_{MEMS} = Q/\pi f^r$ under the assumption of ideal harmonic oscillator³⁹ (Q is the quality factor of the MEMS
 494 device, f^r is the MEMS resonant frequency). With $Q = 20$, $f^r = 1\text{kHz}$, $t_{MEMS} \sim 6\text{ms}$.

495 Computation time for modulated scanning pattern design depends on multiple factors: complexity of RoI weight map (W
 496 in main text, Equation 4), number of iteration steps and the initialization strategy. The weight map can take float values as in
 497 the depth completion task (Figure 7), or binary values as in the 3D object detection task discussed in the main text (Figure
 498 3(c)). This choice of RoI weight map parameters depends on the format of input RoI. In 3D object detection task, the RoIs
 499 are given as the 2D object bounding boxes estimations. Therefore, binary RoI weight map is sufficient to represent these simple
 500 geometric shapes.

501 With binary RoI weight map, the convergence of optimization framework is much faster and each optimization step size
 502 can be larger, compared to that shown in Figure 7. When started from a random initialization, the algorithm usually takes 10
 503 to 20 iteration steps to achieve convergence. Figure 9(a) shows a typical convergence curve. We implement the optimization
 504 algorithm with PyTorch (for automatic gradient descent) and run it on Intel Core i7 CPU (Macbook Pro). Each iteration takes
 505 $\sim 2.5\text{ms}$ and the total optimization time is $\sim 25\text{-}50\text{ms}$. We expect better implementation and more powerful hardware to
 506 increase the speed of single optimization iteration.

507 Although the pattern transition time delay roughly satisfies real-time operation requirement (30 FPS), we can further re-
 508 duce the time delay for higher speed systems. One of the key insight is that real-world scenes change smoothly. Therefore,
 509 a Kalman filter-type prediction algorithm can be utilized to compensate for the time delay. Similar approaches are widely
 510 applied in LiDAR data stream processing pipelines^{40,41}. Also, since regions-of-interest in successive frames overlap signifi-
 511 cantly, optimized patterns should also be similar. Therefore, we can use the optimization result in the previous frame as the
 512 initialization in current frame optimization. Preliminary experiments show that usually less than 5 iteration steps is needed

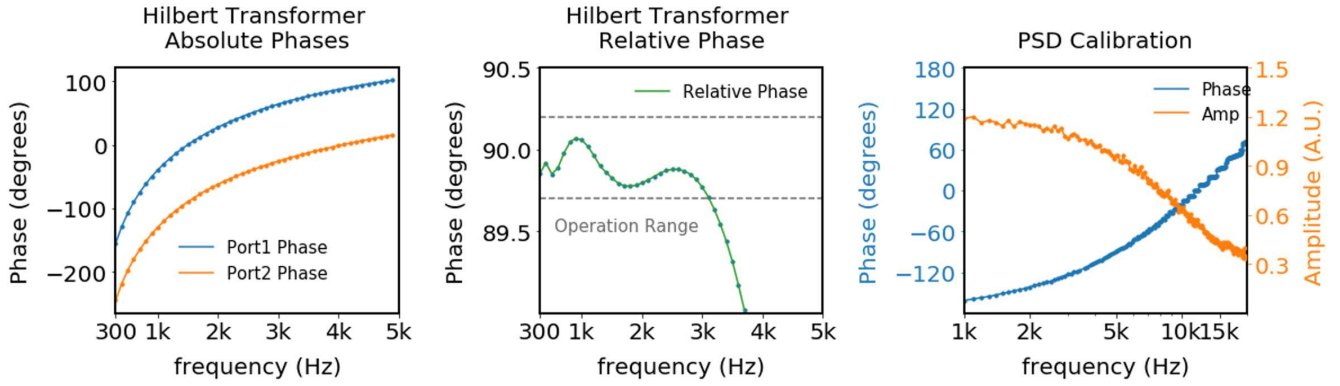


Figure 10. (a) Phase response of port1 and port2 on Hilbert transformer boards. (b) Relative phase between the two ports are within 90 ± 0.3 degrees in the operation range of 300 – 3000 Hz. This range can be adjusted through changing resistance values in the circuit. (c) Phase and amplitude response of position sensor (PSD).

513 for convergence, in contrast to ~ 20 iterations when the optimization is randomly initialized. Detailed discussions on these
 514 algorithm improvements are out of the scope of the current paper and we leave them for future work.

515 Experimental details

516 Calibrations on phase control system

517 Phase calibration for elements in the control system is required for compensation during the system operation. Calibrations on
 518 Hilbert transformer board and position sensor (PSD) are shown in Figure 10. All calibrations are conducted with a high speed
 519 oscilloscope. As shown in Figure 10(b), the relative phase between port1 and port2 of Hilbert transformer board is within
 520 90 ± 0.3 degrees range in the operational range of 300 – 3000Hz.

521 Phase uncertainty of MEMS scanner

522 Amplitudes and phases of transfer function $H_x(f_x)$, $H_y(f_y)$ are shown in Figure 11(a),(b), for two scanning axis of the MEMS
 523 scanner. From the calibration, resonant frequency of MEMS scanner is determined to be $f_x^r = 2660\text{Hz}$, $f_y^r = 1100\text{Hz}$. Quality
 524 factors are determined from full-width-half-maximum (FWHM) on the transfer function curve, $Q_x \sim 30$, $Q_y \sim 50$. As shown
 525 in Figure 11(a),(b), around resonance, relative phase between MEMS scanner motion and the input actuation signal undergoes
 526 a steep transition. Small fluctuations in the resonant frequency would result in large phase changes. This small fluctuation can
 527 be due to temperature fluctuations, spring stiffening and other random environmental factors.

528 We characterize this phase uncertainty of MEMS scanner when control system is NOT used. We record the relative phase
 529 between the x-axis actuation signal and scanner motion within 40minutes. The MEMS scanner is actuated at a fixed frequency
 530 2660 Hz. No modulation or control are used. Since the phase of actuation signal (from signal generator) is assumed to be
 531 stable enough, we attribute the $\sim 10^\circ$ relative phase change, shown in Figure 11(c), to fluctuations in MEMS scanner.

532 Power consumption

533 The power consumption of proposed MEMS scanner system can be divided into two parts: control circuit power consumption
 534 and MEMS actuation power consumption. Here we give a detailed calculation:

535 The proposed control circuit consists of 4 operational amplifiers (Op-Amps), 2 for each scanning direction control. This
 536 contributes the major power consumption for the control circuit. During operation, each Op-Amp consumes $\sim V_{cc} \times I_{cc}$ power,
 537 where V_{cc} is the supply voltage and I_{cc} is the drain current. To achieve a low power consumption, Op-Amp such as TL062 can
 538 be used, with drain current as low as $200\mu\text{A}$ while still operates up to +30 Volts single supply.

539 The power consumption of a MEMS device can be expressed as $2\pi f C V_{rms}^2$, where f is actuation frequency, C is the
 540 capacitor of MEMS and V_{rms} is the RMS(root-mean-square) actuation voltage. Since an electrostatically actuated MEMS
 541 device usually has a capacitor $< 1\text{pF}$, and the actuation voltage is in the order of 10-100V, the MEMS device consumes a
 542 very small amount of power, in the order of nW to μW . Therefore, to apply such a scanner on portable/mobile devices, the
 543 major physical constraint is the maximum amplitude of actuation voltage, instead of the power consumption. When operating
 544 off-resonance and maximum actuation voltage is fixed, the scanning range decreases. This physical constraint is ignored in
 545 previous designs and motivates a more complete one proposed in this paper.

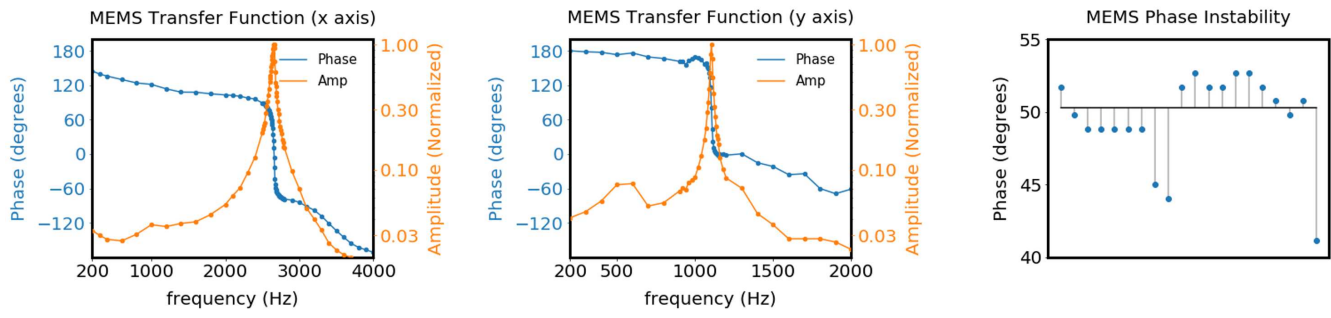


Figure 11. (a),(b) Transfer function amplitudes and phases for the used MEMS scanner. Quality factors $Q_x \sim 30$ and $Q_y \sim 50$ can be estimated from full-width-half-maximum (FWHM) on the H_x, H_y curves. (c) Phase uncertainty of MEMS scanner. Relative phase between MEMS scanner motion and input actuation signal can be unstable due to random fluctuations in the system. An example is shown with 2660 Hz actuation. Relative phase changes can be as large as $\sim 10^\circ$ within 40 minutes time range.